First-Photon Imaging

Ahmed Kirmani,[1]* Dheera Venkatraman,[1] Dongeek Shin,[1] Andrea Colaço,[1] Franco N. C. Wong,[1] Jeffrey H. Shapiro,[1] Vivek K Goyal[1,2]*

Imagers that use their own illumination can capture three-dimensional (3D) structure and reflectivity information. With photon-counting detectors, images can be acquired at extremely low photon fluxes. To suppress the Poisson noise inherent in low-flux operation, such imagers typically require hundreds of detected photons per pixel for accurate range and reflectivity determination. We introduce a low-flux imaging technique, called first-photon imaging, which is a computational imager that exploits spatial correlations found in real-world scenes and the physics of low-flux measurements. Our technique recovers 3D structure and reflectivity from the first detected photon at each pixel. We demonstrate simultaneous acquisition of sub–pulse duration range and 4-bit reflectivity information in the presence of high background noise. First-photon imaging may be of considerable value to both microscopy and remote sensing.

The capture of three-dimensional (3D) structure and reflectivity using an active imager when the back-reflected optical flux reaching the detector approaches a few photons per pixel has many applications (1–3). Imagers for such applications typically use Geiger-mode avalanche photodiodes (APDs), which can time-resolve single-photon detections with jitters of a few tens of picoseconds (4). Transverse spatial resolution is typically obtained point by point by using raster-scanned illumination and a single detector (5) or with floodlight illumination and a spatially resolving detector array (6).

In 3D light detection and ranging (LIDAR) systems (3, 7), the scene is illuminated with a stream of laser pulses, the back-reflected light is detected with a Geiger-mode APD, pixel-by-pixel range information is obtained from histograms of the time delays between transmitted and detected pulses (8), and pixel-by-pixel relative reflectivity is found from the number of photons detected in a fixed dwell time. Tens of photon detections per pixel suffice for accurate range imaging when background light is inconsequential, despite the Poisson noise inherent in photon counting (9, 10). Hundreds of photons, however, are needed for accurate reflectivity imaging, even in the absence of background light. Similar numbers are necessary for range imaging when detections arising from background light lead to anomalous range values (11, 12). In first-photon imaging, we capture 3D spatial structure and reflectivity by using only the first photon detection at each pixel. It is a computational method for low-flux imaging that produces high-quality range images, despite the presence of high background noise, and high-quality reflectivity images, when a conventional reflectivity image built from one photon detection per pixel would be featureless. These results

derive from exploiting the spatial correlations present in real-world scenes within a computational framework matched to the physics of low-flux measurements.

For each pixel, our imager used the number of illumination pulses before the first photon detection as an initial reflectivity estimate. Poisson noise precludes these pixel-by-pixel estimates from providing a high-quality reflectivity image. We suppressed that noise by exploiting the high degree of spatial correlation in real-world scenes; that is, that neighboring pixels have strong distance and reflectivity correlations punctuated by sharp boundaries. Such correlations can be captured through a Markov random field (13) or sparsity in the scene's discrete wavelet transform (DWT) coefficients (14, 15). We suppressed Poisson noise in the

reflectivity image by means of a DWT-based regularization. We also exploited spatial correlations to censor anomalous range values from an initial pixel-by-pixel range image.

Our setup (Fig. 1) consists of a pulsed laser source illuminating a scene with quasi-Lambertian reflectivity in a raster-scanned manner and an incandescent lamp that injects background light. Back-reflected laser light plus background light was collected by a Geiger-mode APD providing time-resolved single-photon detections. Each spatial location (pixel), (x, y), was illuminated with a periodic stream of laser pulses until the first photon was detected. We recorded the first detected photon's arrival time, $t(x, y)$, relative to the most recently transmitted pulse, along with the number of pulses, $n(x, y)$, that were transmitted before that detection. The lamp's optical power was adjusted so that each first-photon detection had about 50% probability of originating from background light.

The first-photon data were used to reconstruct scene reflectivity, $\alpha(x, y)$, and 3D spatial structure, $Z(x, y)$, via the following three-step procedure. First, we connected the statistics of $n(x, y)$ to $\alpha(x, y)$. Let S be the average photon number in the back-reflected signal received from a single laser pulse illuminating a unity-reflectivity spatial location, B denote the arrival rate of background photons at the detector (16), T_r be the pulse repetition period, and γ be the imager's photodetection efficiency. The probability of not detecting a photon when pixel (x, y) is illuminated by a single laser pulse is (16)

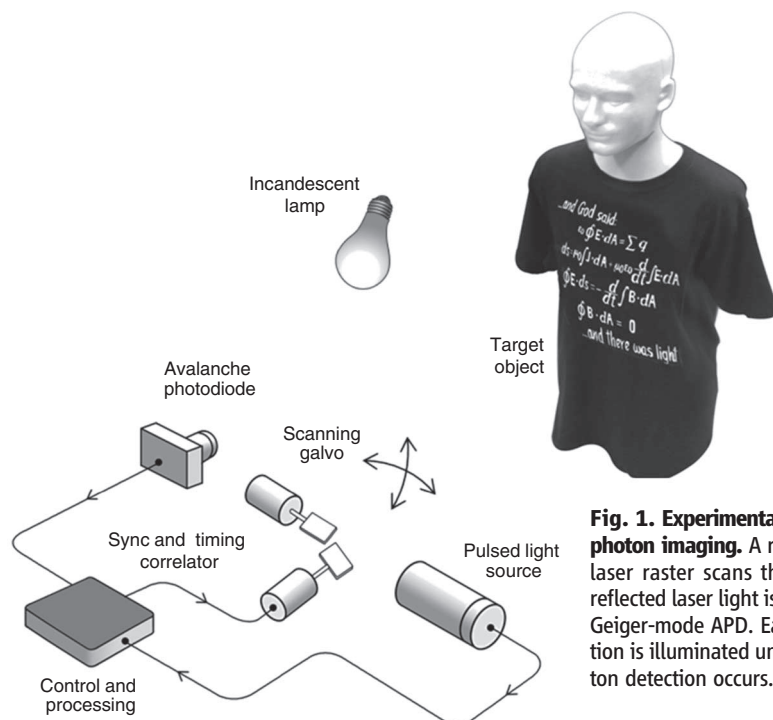$$P_0(x,y) = e^{-\gamma[\alpha(x,y)S + BT_r]}$$

Fig. 1. Experimental setup for first-photon imaging. A repetitively pulsed laser raster scans the scene. Back-reflected laser light is detected with a Geiger-mode APD. Each spatial location is illuminated until the first photon detection occurs.

[1]Research Laboratory of Electronics, Massachusetts Institute of Technology, Cambridge, MA 02139, USA. [2]Department of Electrical and Computer Engineering, Boston University, Boston, MA 02215, USA.

*Corresponding author. E-mail: akirmani@mit.edu (A.K.); v.goyal@ieee.org (V.K.G.)

Because each transmitted pulse gives rise to independent Poisson noise, $n(x,y)$ has the geometric distribution

$$\Pr[n(x,y) = k] = P_0(x,y)^{k-1}[1 - P_0(x,y)],$$

$$\text{for } k = 1, 2, \dots \quad (1)$$

In the absence of background light, the pointwise maximum-likelihood reflectivity estimate, $\widehat{a}_{\text{ML}}(x,y)$, is proportional to $1/n(x,y)$ for $n(x,y) >> 1$ (16). However, background illumination severely corrupts these pointwise estimates (Fig. 2, A to C). Our imager exploits spatial correlations to accurately reconstruct scene reflectivity by maximizing the product of data likelihoods (Eq. 1) over all spatial locations combined with a sparsity-promoting regularization function, namely the sum of absolute values of the image's DWT coefficients (16). The resulting global optimization problem is strictly convex (16); thus, a unique optimal reflectivity estimate is readily obtained from standard numerical solvers (17, 18).

The pointwise range estimate from a first-photon detection is $\widehat{Z}(x,y) = ct(x,y)/2$ for a transmitted pulse whose peak is at time $t = 0$, where c is the speed of light. Its root mean square (RMS) estimation error is $(c/2)\sqrt{(T_p^2 + T_r^2/12)/2}$ in the presence of background light (16), where $T_p << T_r$ is the laser pulse's RMS time duration and the 1/12 factor comes from the uniformly distributed nature of the background-generated detections. Direct application of a spatial-correlation regularization to maximizing time-of-arrival likelihoods is infeasible, because background light makes the optimization objective function multi-modal. Background light also causes pointwise methods to fail (Fig. 2, A to C), so we used spatial correlations to censor $t(x,y)$ values that are range anomalies.

Anomalous detections have arrival times that are uniformly distributed over the time interval $[0, T_r]$ and mutually independent over spatial locations, so that they have high variance $T_r^2/12$ relative to that of back-reflected laser-pulse (signal) detections, which are temporally concentrated and spatially correlated. Let $s(t)$ be the normalized $[\int_0^{T_r} s(t)dt = 1]$ photon-flux waveform of the laser pulse emitted at $t = 0$. At low optical flux, that is, when $\gamma(S + BT_r) << 1$, and the first photon detected from location (x,y) is a signal photon, then the probability density function for $t(x,y)$ is (16)

$$p_{t(x,y)}(\tau) = s(\tau - 2Z(x,y)/c), \text{ for } 0 \leq \tau \leq T_r$$

$$(2)$$

which has variance $T_p^2 << T_r^2/12$, regardless of the reflectivity at (x, y). The high degree of spatial correlation in the scene's 3D structure then implies that signal-generated photon arrival times have much smaller conditional variance, given data from neighboring locations, than do anomalous detections. Step 2 of the computational imager uses this statistical separation to censor background-generated arrival times from an initial pixel-by-pixel range image.

For each spatial location, a rank-ordered absolute differences statistic (19) is computed by using the photon arrival times of its eight nearest neighbors (16). Then, a binary hypothesis test—whose decision threshold is dependent on the reflectivity estimate from step 1—identifies, with high probability, whether the photon detection was due to signal or background (Fig. 2, G to I), allowing us to delete nearly all anomalous range values.
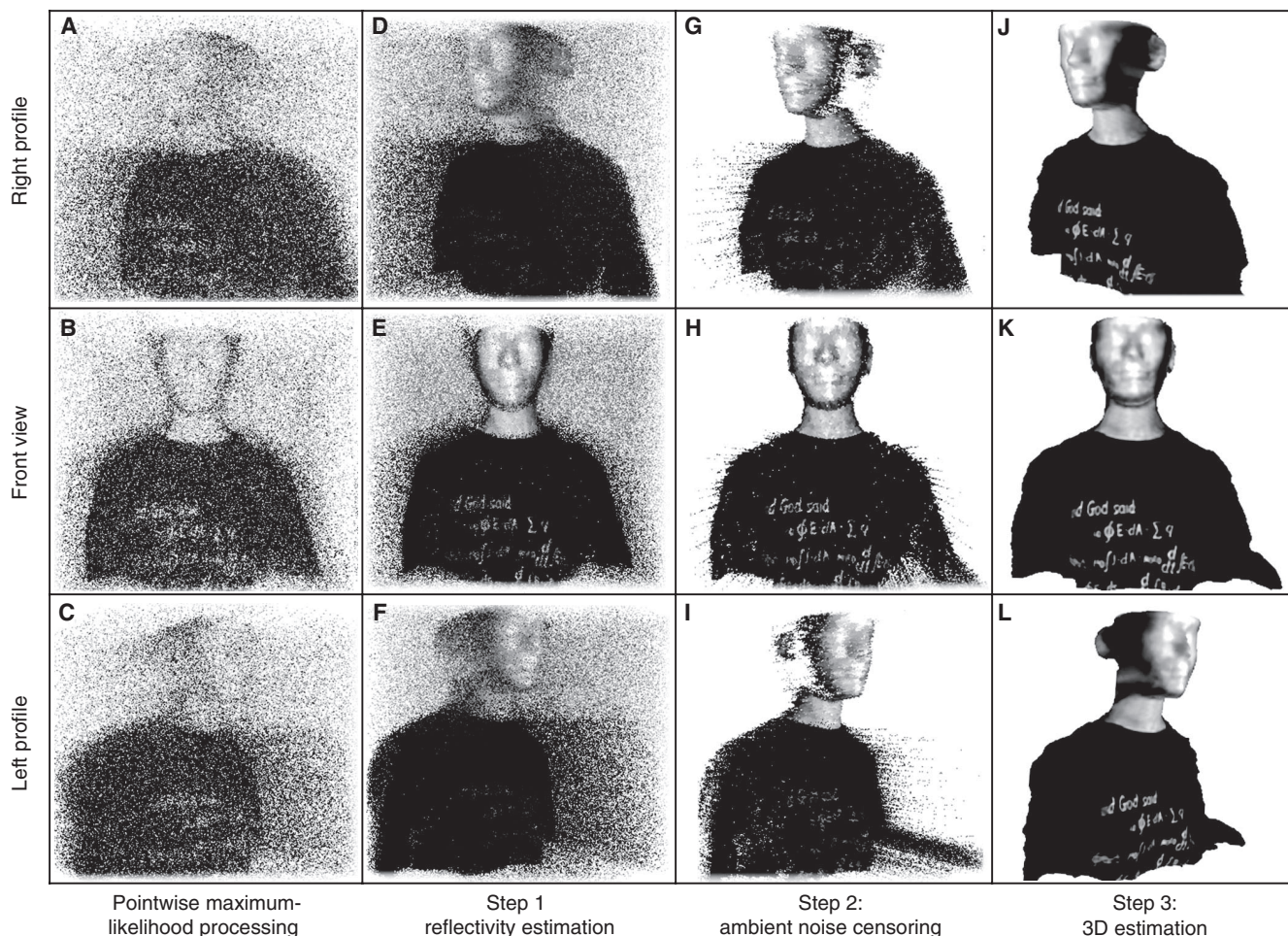

Fig. 2. Computational first-photon 3D and reflectivity reconstruction. (A to L) 3D estimates of front views and lateral views rendered as point clouds overlaid with reflectivity data.

Once background detections have been rejected, 3D estimation using photon arrival times, $\{t(x, y)\}$ becomes tractable. Our final processing step computes the regularized maximum-likelihood 3D estimate by maximizing the product of data likelihoods (Eq. 2), over the uncensored spatial locations, combined with a DWT-based penalty function that exploits spatial correlations present in a scene's 3D structure (16).

After radiometric calibration, we tested first-photon imaging on scenes with both geometric and reflectivity complexity. One object investigated was a life-sized mannequin with white polystyrene head and torso donned with a black cotton shirt imprinted with white text. The approximate dimensions of the head were 20 cm by 16.5 cm by 24 cm, and those of the torso were 102 cm by 42 cm by 29 cm. The mannequin was placed at a range of 1.5 m from the imaging setup. By using the first-photon data, we estimated the object reflectivity and 3D spatial form as described above. For a 1-megapixel reflectivity and 3D reconstruction, our data acquisition time was about 20 min, and the computations took less than 3 min on a desktop computer. A standard graphics package was then used to visualize the object's 3D profile, overlaid with reflectivity data, after each processing step (Fig. 2, D to L, and movie S1).

Our first-photon imager recovers a great deal of object detail. Figures 2, D to F, and 3 show recovery of reflectivity information—including text, facial features, surface reflectivity variations, and specular highlights—that are heavily obscured in pointwise maximum-likelihood estimates. As shown in Fig. 2, G to I, background-detection censoring affords substantial improvement in range estimation, so that the reconstructed 3D form reveals fine structural features, such as the nose, eyes, and lips (Fig. 2, J to L).

To quantify the accuracy of our approach, we compared the 3D reconstruction of the mannequin head with a 3D image captured with our imaging setup operating as a direct-detection LIDAR. For this reference capture, background light was first reduced to negligible levels, after which ~1000 photon detections were recorded at each spatial location. Pointwise 3D estimates were then obtained from a photon-counting histogram. This data-intensive baseline technique allows sub-mm-accuracy 3D reconstruction for our T_p= 226 ps value (20).

Figure 4 shows superimposed facial profiles from the two methods. Both 3D forms were measured by using the same imaging setup, obviating the need for registration or scaling. The RMS error of our computational imager was slightly lower than 3.5 mm, with higher values near the edge of the mannequin and around the sides of the nose and the face. These locations have surface normals that are nearly perpendicular to the line of sight, which dramatically reduces their back-reflected signal strength relative to background light. Consequently, they incur more anomalous detections than do the rest of the pixels. Although

our method censors range anomalies near edges, it estimates the missing ranges by using spatial correlations, leading to loss of subtle range details at these edges.

The range resolution of our computational imager was measured with a test target and found to be about 4 mm (figs. S2 to S5). This resolution is 8.5 times smaller than $cT_p/2 = 34$ mm (our

setup's RMS error for pointwise first-photon range estimation in the absence of background light) and 765 times smaller than $(c/2)\sqrt{(T_p^2 + T_r^2/12)/2} = 3.06$ m (our setup's RMS error for pointwise first-photon range estimation in the presence of background light) (16). Moreover, LIDAR-mode pointwise range estimation from a photon-counting histogram required at least 115 photons per pixel
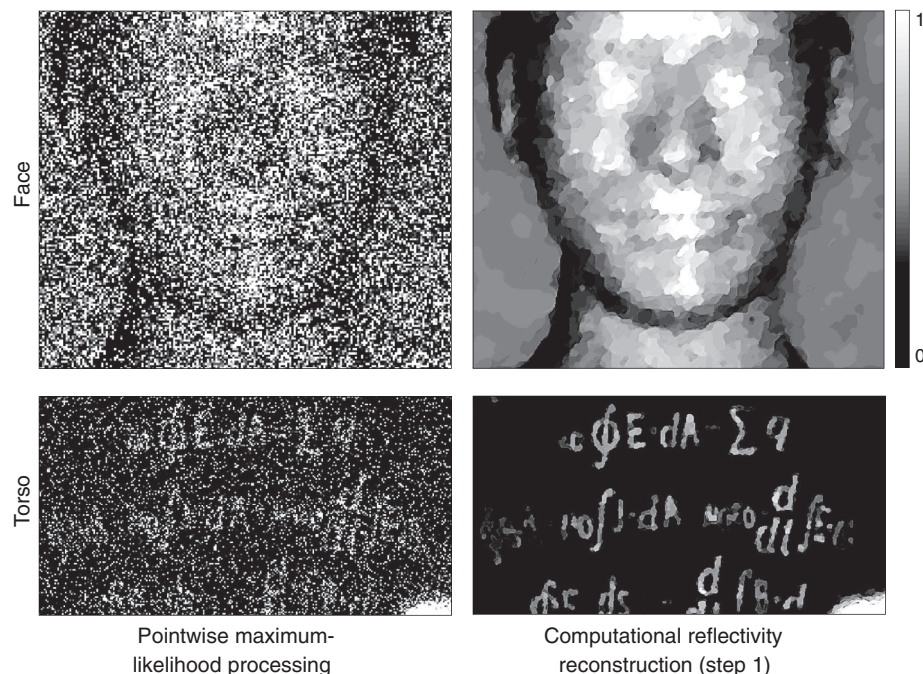

Fig. 3. Reflectivity reconstruction from first-photon detections. The scale quantifies reflectivity relative to that of a high-reflectivity calibration point, $\alpha(x_{ref}, y_{ref})$, on a 0 to 1 scale.
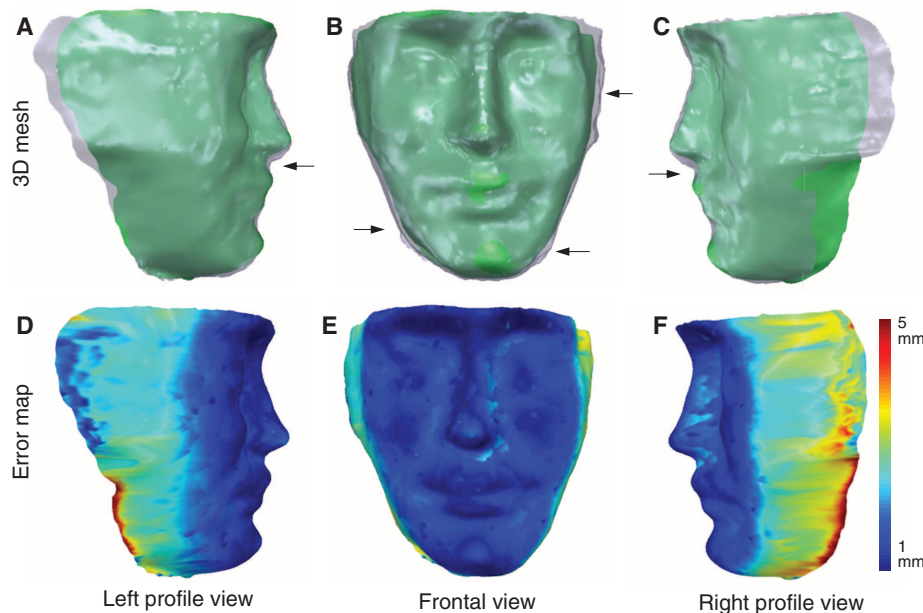

Fig. 4. Comparison between computational first-photon 3D imager and LIDAR system. Rendered views of the facial surfaces reconstructed with computational imaging (gray) and 3D LIDAR (green) are shown in frontal (**B**) and lateral (**A**) and (**C**) profiles with arrows indicating the locations of significant range discrepancies. Color-coded absolute pointwise differences between the two surfaces, overlain on the LIDAR reconstruction, are shown in (**D**) to (**F**).

to achieve a 4-mm RMS error under identical imaging conditions.

Reflectivity measurements with a test pattern showed that our method provided at least 4 bits of information; that is, 16 linear gray-scale levels could be distinguished (figs. S6 to S9). We also tested the repeatability of our method by collecting 500 independent first-photon data trials for the mannequin. We found our first-photon imager to consistently demonstrate qualitative and quantitative improvement over pointwise processing (movie S2). Its performance was also reproducible with other real-world scenes composed of multiple distinct objects at different ranges (figs. S10 to S12).

For completeness, we compared our imager with image-denoising techniques. One such method median filters the pointwise estimates (Fig. 2, A to C). Its reduction of noise resulting from anomalous detections comes at the expense of image oversmoothing, which leads to loss of perceptual information contained in edges, reflectivity, and structural variations. State-of-the-art denoising algorithms, like BM3D (21), exploit spatial correlations to mitigate high levels of noise, but they fail to match the performance of our imager because first-photon detection statistics differ from the conventional noise models that such algorithms presume (figs. S13 and S14).

Our computational first-photon imaging technique achieves its high-quality performance by using spatial correlations to suppress Poisson noise in reflectivity images and censor range anomalies from arrival-time data. It extracts more information from the collection of single detections than state-of-the-art active imagers would. Thus, it allows laser power to be reduced without sacrificing image quality, something that can be crucial for biological applications, such as fluorescence-lifetime imaging (22, 23). It also enables remote sensing at longer standoff distances with power-limited transmitters and could be combined with techniques for detecting multiple depths per pixel (24). The system we have demonstrated can be improved with better background-light suppression (25), range gating (26), and advances in single-photon detector technology (27, 28).

References and Notes

1. J. C. Nicolas, *J. Biolumin. Chemilumin.* **9**, 139–144 (1994).
2. W. Becker *et al.*, *Microsc. Res. Tech.* **63**, 58–66 (2004).
3. A. McCarthy *et al.*, *Opt. Express* **21**, 8904–8915 (2013).
4. N. Savage, *Nat. Photonics* **3**, 738–739 (2009).
5. G. S. Buller, A. M. Wallace, *IEEE J. Sel. Top. Quantum Electron.* **13**, 1006–1015 (2007).
6. M. Jack *et al.*, *Proc. SPIE* **8033**, 80330M (2011).
7. B. Schwarz, *Nat. Photonics* **4**, 429–430 (2010).
8. Y. Chen, J. D. Müller, P. T. C. So, E. Gratton, *Biophys. J.* **77**, 553–567 (1999).
9. S. Pellegrini, G. S. Buller, J. M. Smith, A. M. Wallace, S. Cova, *Meas. Sci. Technol.* **11**, 712–716 (2000).
10. A. McCarthy *et al.*, *Opt. Express* **21**, 22098–22113 (2013).
11. D. L. Snyder, *Random Point Processes* (Wiley, New York, 1975).
12. M. E. O'Brien, D. G. Fouche, *Lincoln Lab. J.* **15**, 37 (2005).
13. S. Geman, D. Geman, *IEEE Trans. Pattern Anal. Mach. Intell.* **PAMI-6**, 721–741 (1984).
14. B. A. Olshausen, D. J. Field, *Netw. Comput. Neural Syst.* **7**, 333–339 (1996).
15. A. Srivastava, A. B. Lee, E. P. Simoncelli, S.-C. Zhu, *J. Math. Imaging Vis.* **18**, 17–33 (2003).
16. Supplementary materials are available on *Science* Online.
17. S. P. Boyd, L. Vandenberghe, *Convex Optimization* (Cambridge Univ. Press, Cambridge, 2004).
18. Z. T. Harmany, R. F. Marcia, R. M. Willett, *IEEE Trans. Image Process.* **21**, 1084–1096 (2012).
19. R. Garnett, T. Huegerich, C. Chui, W. He, *IEEE Trans. Image Process.* **14**, 1747–1754 (2005).
20. A. M. Wallace, G. S. Buller, A. C. Walker, *Comput. Control Eng. J.* **12**, 157–168 (2001).
21. K. Dabov, A. Foi, V. Katkovnik, K. Egiazarian, *IEEE Trans. Image Process.* **16**, 2080–2095 (2007).
22. W. Jiang, M. L. Baker, Q. Wu, C. Bajaj, W. Chiu, *J. Struct. Biol.* **144**, 114–122 (2003).
23. C.-W. Chang, M.-A. Mycek, *Proc. SPIE* **7570**, 757007 (2010).
24. S. Hernández-Marín, A. M. Wallace, G. J. Gibson, *IEEE Trans. Pattern Anal. Mach. Intell.* **29**, 2170–2180 (2007).
25. M. A. Albota *et al.*, *Appl. Opt.* **41**, 7671–7678 (2002).
26. J. Busck, H. Heiselberg, *Appl. Opt.* **43**, 4705–4710 (2004).
27. G. N. Gol'tsman *et al.*, *Appl. Phys. Lett.* **79**, 705 (2001).
28. S. Chen *et al.*, *Appl. Opt.* **52**, 3241–3245 (2013).

Direct Stereospecific Synthesis of Unprotected N-H and N-Me Aziridines from Olefins

Jawahar L. Jat,[1] Mahesh P. Paudyal,[1] Hongyin Gao,[1] Qing-Long Xu,[1] Muhammed Yousufuddin,[2] Deepa Devarajan,[3] Daniel H. Ess,[3]*† László Kürti,[1]*† John R. Falck[1]*†

Despite the prevalence of the N-H aziridine motif in bioactive natural products and the clear advantages of this unprotected parent structure over N-protected derivatives as a synthetic building block, no practical methods have emerged for direct synthesis of this compound class from unfunctionalized olefins. Here, we present a mild, versatile method for the direct stereospecific conversion of structurally diverse mono-, di-, tri-, and tetrasubstituted olefins to N-H aziridines using O-(2,4-dinitrophenyl)hydroxylamine (DPH) via homogeneous rhodium catalysis with no external oxidants. This method is operationally simple (i.e., one-pot), scalable, and fast at ambient temperature, furnishing N-H aziridines in good-to-excellent yields. Likewise, N-alkyl aziridines are prepared from N-alkylated DPH derivatives. Quantum-mechanical calculations suggest a plausible Rh-nitrene pathway.

Aziridines, the triangular, comparably highly strained nitrogen analogs of epoxides, are important synthetic intermediates (i.e., building blocks) en route to structurally complex molecules because of their versatility in myriad regio- and stereoselective transformations (ring openings and expansions, as well as rearrangements) (1–6). The aziridine structural motif, predominantly N-H and to a lesser extent N-alkyl, also appears in biologically active natural products (e.g., azinomycins and mitomycins) (7–9). As a result, the synthesis and chemistry of aziridines have been the subject of intense research during the past 25 years, resulting in multiple aziridination methods (10–23). Most of these methods rely either on the transfer of substituted nitrenes, which are generated by using strong external oxidants, to the C=C bond of olefins or the transfer of substituted carbenes to the C=N bond of imines. Normally, the result is an aziridine bearing a strongly electron-withdrawing N-protecting group (e.g., Ts: *para*-toluenesulfonyl; Ns: *para*-nitrophenylsulfonyl); removal of these *N*-sulfonyl protecting groups is problematic as it often results in the undesired

[1]Division of Chemistry, Department of Biochemistry, University of Texas Southwestern Medical Center, Dallas, TX 75390, USA. [2]Center for Nanostructured Materials, University of Texas at Arlington, Arlington, TX 76019, USA. [3]Department of Chemistry and Biochemistry, Brigham Young University, Provo, UT 84602, USA.

*These authors contributed equally to this work.
†Corresponding author. E-mail: laszlo.kurti@utsouthwestern.edu (L.K.); j.falck@utsouthwestern.edu (J.R.F.); dhe@chem.byu.edu (D.H.E.)